Chalcogenide Letters Vol. 22, No. 3, March 2025, p. 261 - 276

Impedance spectroscopy insights into $(NiO)_{(0.5)}/(Fe_2O_3)_{(0.5)}$@C@$MoS_2$ nanofibers composite for tunable EMI shielding applications

U. Anwar [a], N. A. Noor [b], S. Mumtaz [c,*], I. M. Moussa[d]
[a] *Institute of Chemical Sciences, Bahauddin Zakariya University, Multan 60000, Pakistan*
[b] *Department of Physics, University of Sargodha, 40100, Sargodha, Pakistan*
[c] *Department of Chemical and Biological Engineering, Gachon University, 1342 Seongnamdaero, Sujeong-gu, Seongnam-si 13120, Republic of Korea*
[d] *Department of Botany and Microbiology, College of Science, King Saud University, P.O. Box 2455, Riyadh, 11451, Saudi Arabia*

The combination of two-step synthesis processes is employed for the fabrication of $(NiO)_{(0.5)}/(Fe_2O_3)_{(0.5)}$@C@$MoS_2$ (NFCM) nanofibers composite through electrospinning and hydrothermal techniques. This nanofiber composite is designed for tunable dielectric materials and electromagnetic interference (EMI) shielding applications. Using impedance spectroscopy, the electrical properties of an NFCM pellet are analyzed using an equivalent circuit model (R_1Q_1), with a primary focus on the variation of relaxation time with frequency at different temperatures. Utilizing the Mott. variable range hopping (MVRH) model, and small polaronic hopping model, the localization length of the hoping carriers is determined to be 0.98 Å and the activation energy of thermally activated charge carriers is determined to be (E_a=.0.27eV). The activation energy calculated from the impedance, SPH model, and conductivity plot are inaudibly comparable representing the conduction and relaxation process associated with the same electroactive regions. The (NFCM nanofibers composite exhibits higher conductivity at all temperature ranges, which is a crucial attribute for effective EMI shielding applications. In the X-band frequency range (8.2–12.4 GHz), the calculated EMI shielding effectiveness of NFCM nanofibers composite is 24.25 dB, this qualifies them for use in high frequency applications.

(Received December 22, 2024; Accepted March 25, 2025)

Keywords: EMI shielding, Dielectric constant, Tangent loss, Hydrothermal technique, Impedance spectroscopy, Electrospinning and nanofibers

1. Introduction

In recent decades, there has been a notable increase in the interest in magnetic (core) dielectric (shell) nanofiber materials owing to their distinctive electromagnetic response characteristics and versatile applications in the realm of energy storage materials and electromagnetic shielding [1]. The concurrent presence of dielectric (shell) and magnetic (core) physical characteristics in these materials can be excellently tweaked by adjusting synthesis methods to manipulate the morphology, size, and shape of nanomaterials [2]. The development of novel nanofiber materials with distinct features has garnered substantial attention and proven valuable across a wide spectrum of applications [3]. Among the crucial areas of contemporary research and innovation, electrospun metal oxide nanofibers hold particular significance [4]. One-dimensional (1D) magnetic nanofibers have attracted considerable attention owing to their unique combination of electrical and magnetic capabilities, chemical and thermal stability, and appealing structural features. Various techniques have been devised for the production of composite nanofibers [5], with electrospinning emerging as the most economical method for creating nanofibrous magnetic composites compared to alternative approaches [6]. The composite

* Corresponding author: sohail.ahmed2015@gmail.com
https://doi.org/10.15251/CL.2025.223.261

material $(NiO)_{(0.5)}/(Fe_2O_3)_{(0.5)}$@C is noteworthy for its high conductivity, aligning with the well-established reputation of metals and metalized materials for remarkable EMI shielding capabilities. However, the inherent impedance mismatch of a single magnetic material hinders it from exhibiting exceptional EMI shielding characteristics [7].

Addressing the impedance mismatch inherent in single magnetic materials, an effective strategy involves combining magnetic and carbon-based materials to engineer the core-shell structures or other distinctive configurations [8]. Carbon materials, characterized by their lightweight nature, excellent chemical stability, and electrical conductivity, prove instrumental in mitigating dielectric loss in microwave absorbers [9]. To exemplify, a core-shell heterostructure nanofibers composite, denoted as $(NiO)_{(0.5)}/(Fe_2O_3)_{(0.5)}$@C, was crafted through a sequence of surface etching, carbonization, and electrospinning processes [10]. The demonstrated exceptional EMI shielding performance of this composite underscores its efficacy [11]. In this composite, the magnetic characteristics of the $(NiO)_{(0.5)}/(Fe_2O_3)_{(0.5)}$ core are accentuated, while the presence of the carbon shell not only fortifies the structural integrity of the nanofibers but also provides a robust platform for potential functionalization [12]. These attributes can be strategically harnessed to optimize the scattering properties of nanofiber composites, thereby tailoring EMI shielding across broad frequency ranges [13]. Core-shell nanomaterials, typically characterized by a dielectric shell and magnetic core, are particularly promising candidates for this purpose [14]. The altered properties arising from the interplay between the dielectric shell and magnetic core, or their coexistence, contribute to the high utility of these materials. Given the extensive body of literature on core/shell nanomaterials, current research in the EMI shielding field emphasizes the intricate relationship among defect chemistry, phase coexistence, and interface correlations [15].

In the realm of EMI shielding, recent attention has been directed toward MoS_2, a two-dimensional semiconductor material distinguished by its high conductivity and noncentrosymmetric structure [16]. The amalgamation of its conducting characteristics with its two- dimensional morphology positions MoS_2 as a promising material for a diverse array of electronic and nanoelectronics applications [17]. Notably, despite possessing a certain level of electronic conductivity (10-100 S cm^{-1}), MoS_2 can also form distinctive nanostructures, such as flower-like configurations, endowed with unique surface properties that enhance microwave dispersion [18]. This enhancement is achieved by facilitating numerous microwave reflections and dispersions. Remarkably, at a thickness of 3 mm, the unique heterostructure exhibited a significantly heightened efficacy in EMI shielding within the (X-band) frequency region. Recognizing the advantages of MoS_2, a pragmatic approach involves combining MoS_2 nanocomposite with magnetic materials in a core-shell configuration to tailor electromagnetic properties [19]. Furthermore, the outermost layer, primarily composed of MoS_2, contributes exceptional electrical conductivity, thereby expanding the material's efficiency to shield against EMI a critical requirement in contemporary electronic devices and communication systems.

This study successfully synthesizes an electromagnetic heterostructure nanofiber material, denoted as NFCM, utilizing a straightforward two-step methodology involving electrospinning and hydrothermal techniques. Notably, the $((NiO)_{(0.5)}/(Fe_2O_3)_{(0.5)}$ nanofibers composite represents a distinctive material system wherein nickel oxide (NiO) and iron (III) oxide (Fe_2O_3) coexist within a well-defined nanostructured architecture. This unique composition serves as a robust platform for the exploration of multifunctional properties, particularly in the realm of electrical characteristics. The EMI shielding attributes of NFCM, the temperature and frequency-dependent conduction mechanisms within electro-active regions present in the nanofiber materials, and the coexistence of NiO/Fe_2O_3 metal oxide nanofibers materials have not been hitherto reported. Impedance spectroscopy is a key device used to clarify the temperature and frequency-dependent conduction mechanisms of the heterostructure nanofiber materials, providing information about the source of their EMI shielding properties.

The synthesis, structural characterization, and subsequent electrical property modulation of NFCM nanofiber composites are thoroughly examined in this work. The primary objective of most EMI shielding research is to diminish electromagnetic radiation within specific frequency ranges. Temperature and frequency-dependent impedance spectroscopy (IS) are employed to

investigate the electrical properties of NFCM nanofiber composite. This method provides valuable insights into the frequency and mobility of charge carriers. However, an understanding of charge carrier mobility derived from impedance dimensions and the conduction mechanism within the low-frequency realm holds promise for comprehending the variation of EMI shielding presentation. The association of electrical characteristics, dielectric constant, conductivity, and tangent loss with the EMI shielding properties of the NFCM heterostructure nanofibers composite contributes to a comprehensive understanding. A detailed comprehension of the electrical properties facilitates a comparative analysis of EMI shielding properties within a broad frequency range.

2. Experimental

2.1. Materials

The materials employed in this study included Polyvinylpyrrolidone, nickel nitrate hexahydrate iron (III) nitrate nonahydrate, glucose, urea, thiourea ($SC(NH_2)_2$), ammonium molybdate, N, N-dimethylformamide (DMF), and ethanol. All chemicals were sourced from Sigma-Aldrich, possessing the highest available purity, and utilized without further purification. Deionized (DI) water was exclusively employed for solution preparation.

2.2. Preparation of $(NiO)_{(0.5)}$ /$(Fe_2O_3)_{(0.5)}$ nanofibers

The fabrication of nanofibers, ranging in size from nanometers to micrometers, is achieved through the electrospinning process. At ambient temperature, an electrospinning solution is organized by dissolving 8% by weight of PVP in a mixture of 40 mL of DMF, and 60 mL of isopropanol, resulting in a 9% by-weight solution. This solution undergoes magnetic stirring for one hour. Subsequently, the solution is combined with 50% by weight of iron nitrate nonahydrate and 50% by weight of nickel nitrate hexahydrate after which it is stirred for 12 hours, yielding a clear mixture [14]. The resultant solution is then loaded into a 10-milliliter syringe and injected to a multi-needle spinneret. The distance between the needle tip and the aluminum foil collecting plate is maintained at 10 centimeters. Essential parameters for the electrospinning process include a temperature range of 35 to 40 degrees Celsius, relative humidity below 30%, a 12-kilo voltage, and a solution feed rate of five milliliters per hour. The electrically charged solution is elongated over the needle tip under the influence of high voltage applied to the needle tip and the aluminum foil conducting collector plate. This electric field exceeds the surface tension of the droplet, propelling the elongated droplet as a jet near a conducting collecting plate with an opposing charge. As the jet progresses, charged fibers accumulate on the aluminum foil (collecting plate), facilitated by the gradual evaporation of the solvent. Post-collection, the electrospun fibers are thoroughly dried in an oven set at 200 °C for one hour. To produce $(NiO)_{(0.5)}/(Fe_2O_3)_{(0.5)}$ nanofibers, an annealing process is subsequently implemented. The nanofibers undergo annealing at 450 °C for 2 hours, employing a temperature ramping rate of 2 °C min^{-1} [1].

2.3. Preparation $(NiO)_{(0.5)}/(Fe_2O_3)_{(0.5)}$@C composite

To synthesize the $(NiO)_{(0.5)}/(Fe_2O_3)_{(0.5)}$@C nanofibers composite, a solution is prepared by mixing glucose (0.03 moles) and urea (0.3 moles) in 100 mL of water. Subsequently, the previously prepared $(NiO)_{(0.5)}/(Fe_2O_3)_{(0.5)}$@C nanofibers are dispersed in this solution. The resulting mixture is then transferred to a 100 mL Teflon autoclave and subjected to thermal treatment in an oven for 10 hours at 200 °C. The resultant product, denoted as $(NiO)_{(0.5)}/(Fe_2O_3)_{(0.5)}$@C, is subjected to multiple washes with deionized water/ethanol and subsequently dried in a vacuum oven at 50 °C for 10 hours.

2.4. Preparation of $(NiO)_{(0.5)}/(Fe_2O_3)_{(0.5)}$@C@$MoS_2$ composite

In this procedure, a solution is prepared by dissolving 2.5 g of ammonium molybdate and 15.2 g of thiourea in 100 mL of deionized water. A blackish $(NiO)_{(0.5)}/(Fe_2O_3)_{(0.5)}$@C composite powder is introduced into this solution. The resultant mixture is then transferred to a 250 mL Teflon autoclave and subjected to a 24-hour thermal treatment at 200 °C. Following this, the

resulting black precipitates, denoted as NFCM, undergo multiple rinses with deionized water and ethanol before being dried at 40°C [20]. For the determination of crystallite dimensions and phase identification of the NFCM nanofibers composite, X-ray diffractometry is performed using Cu Kα radiation and employing a step size of 0.03 and a scanning speed of 4 min^{-1}.

The nanostructures and morphologies are examined through field emission scanning electron microscopy (FE-SEM). Temperature and frequency-dependent impedance spectroscopy dimensions are conducted using a dielectric analyzer. Pellets are fabricated by squeezing the NFCM powder using a hydraulic press under a pressure of 6 tons for at least three minutes, resulting in pellets with a diameter of 10 mm and a thickness of approximately 2 mm. These pellets undergo a thorough cleaning, and silver gum is applied to equal sides to ensure effective ohmic contact. AC electrical properties are investigated across a wide frequency range (1 Hz-10^7 Hz) within a temperature span of 73 K to 163 K, utilizing an Alpha-N Novo control dielectric analyzer. An AC signal of 0.2 V is applied during these measurements, and a custom-made sample holder containing the pellet is positioned inside a liquid nitrogen Dewar to maintain low temperatures. Furthermore, to assess the EMI shielding ability, materials are crinkled into fine particles, uniformly combined with paraffin at a mass ratio of 1:1, and shaped into slabs measuring 22.4 mm × 10.2 mm. Shielding tests are conducted using a Vector Network Analyzer spanning a frequency range of 10 MHz to 40 GHz.

3. Results and discussion

Fig.1 presents FE-SEM images depicting the morphological characteristics of the samples fabricated in this study. The morphology of the NiO/Fe_2O_3 nanofibers is observed in detail in Fig. 1 (a, b). The average distribution of the diameter of the nanofibers is illustrated in Fig. 1(c), with the average diameter determined using Image J software. These nanofibers exhibit a notable aspect ratio, with lengths extending to several microns and an average diameter of approximately ± 90 nm. Following the carbonization and MoS_2 coating on the surface of the nanofibers, Fig. 2 (a, b) reveals a distinct aggregated nano-flower-like configuration of MoS_2 on the composite material of NiO/Fe_2O_3@C nanofibers core-shell composite [6].

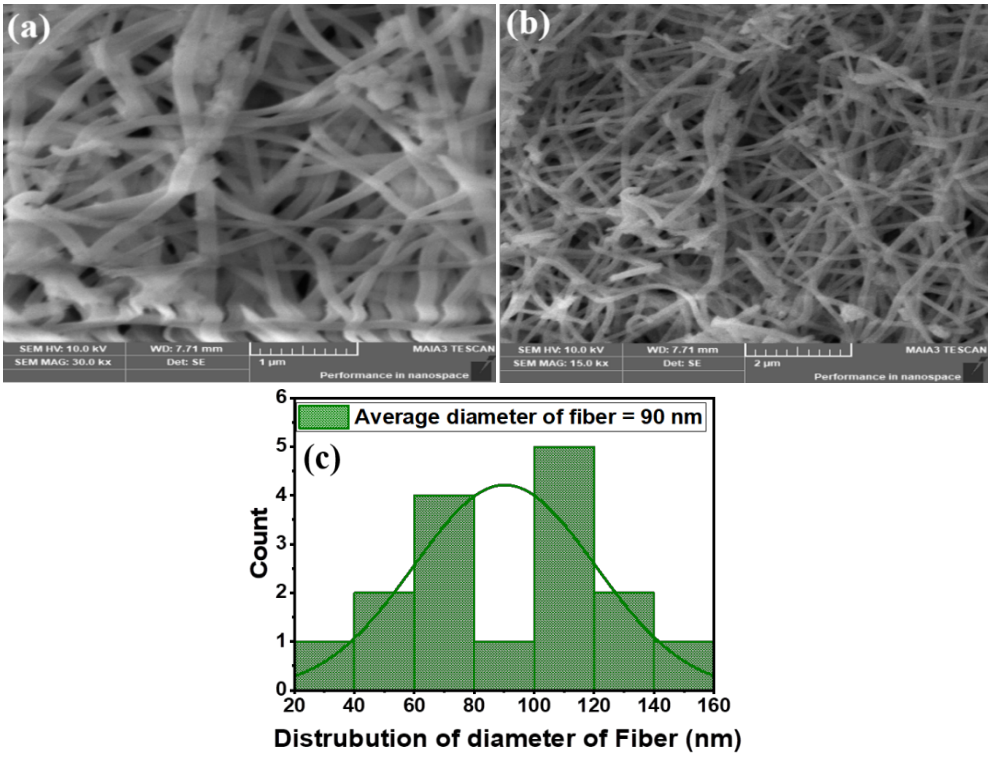

Fig. 1 (a,b) represents the FE-SEM images of $(NiO)_{(0.5)}/(Fe_2O_3)_{(0.5)}$ nanofibers at 15kx and 30kx, and (c) average diameter of fibers.

A substantial quantity of MoS_2 nano-flower uniformly assembles on the surface of the NiO/Fe_2O_3@C nanofiber composite, as illustrated in Fig. 2 (a, b). These nano-flowers, in conjunction with the NFCM nanofibers, collectively form a three-dimensional (3D) conductive network. The surface of the flower-shaped MoS_2 nanostructure is distinguished by a profusion of nano-petals, owing to elevated concentrations of sulfur and molybdenum elements. Notably, these nano-petals exhibit conspicuous aggregation and stacking on the nanofiber's surface. FE-SEM characterization reveals that the limited presence of NiO/Fe_2O_3@C does not compromise the integrity of the 3D flower-like structure, as depicted in Fig. 2 (a, b). The amorphous carbon layer, serving as a bridge between MoS_2 and the NiO/Fe_2O_3 nanofibers, significantly enhances the uniform loading of MoS_2 by providing numerous active sites.

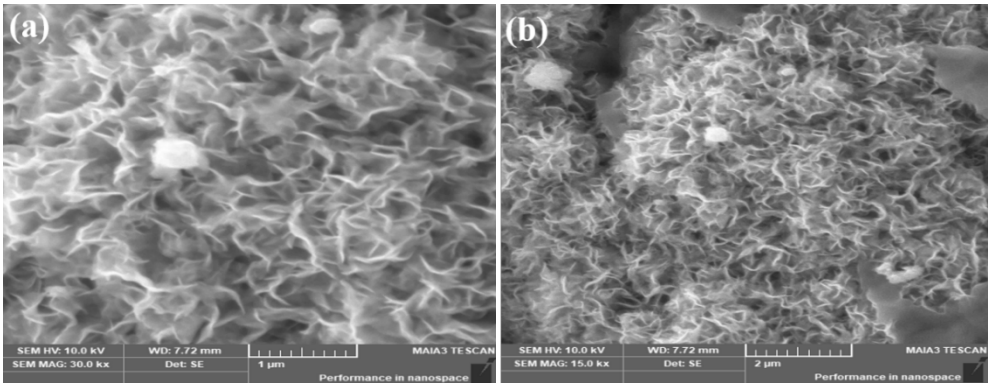

Fig. 2. (a,b) represents the FE-SEM images of NFCM nanofibers composite at 15kx and 30kx.

The XRD patterns of the as-synthesized NFCM nanofibers composite are depicted in Fig. 3. Notably, distinct diffraction peaks are observed at 2θ values of 37.05°, 62.76°, and 79.16°, corresponding to the crystalline planes of (111), (220), and (222), respectively, thereby confirming the presence of NiO nanofibers (Fig. 3). The observed NiO nanofibers align with the known crystallographic pattern (JCPDS 47–1049) [2]. Additionally, the existence of Fe_2O_3 nanofibers is substantiated by diffraction peaks observed at 2θ values of 24.1°, 218 33.1°, 40.7°, 57.6°, and 75.5°, corresponding to the (012), (104), (113), (122), and (220) planes, respectively. These diffraction peaks align with the expected crystallographic pattern for Fe_2O_3 nanofibers (JCPDS: 33-0664) [21]. Furthermore, characteristic peaks at 14.1° and 26° in the XRD patterns are indicative of the presence of carbon and MoS_2, respectively. These distinct peaks affirm the successful incorporation of carbon and MoS_2 components within the nanofiber composite [18].

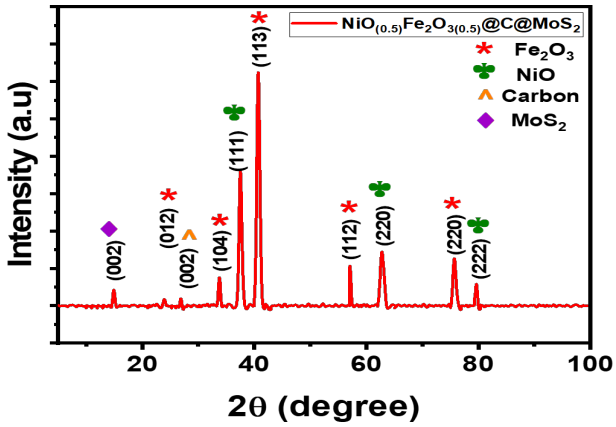

Fig. 3 XRD pattern of NFCM nanofibers composites.

The investigation of the conduction mechanism within heterostructure nanofibers, specifically comprised of $(NiO)_{(0.5)}/(Fe_2O_3)_{(0.5)}$@C@$MoS_2$, is conducted through impedance spectroscopy (IS). Illustrated in Fig. 4 (a) is the impedance plane plot for the nanofiber composites within a low-temperature range (73–163 K). The total resistance of these heterostructure nanofibers is delineated by the intersection of a singular semicircle and a left-side extension, crossing the origin. This singular semicircle indicates the presence of a sole electro-active region within the specified low-temperature range. To enhance the understanding of the conduction mechanism, ZView software is utilized for a comprehensive analysis of impedance plane plots, involving a comparison between empirical data and an analogous electrical circuit.

The impedance plane plot acquired within the temperature zone of 73 K to 163 K is fitted using a single equivalent circuit model, denoted as (R_1Q_1) [2]. The inset of Fig. 4 (a) showcases the parameters, where Q symbolizes the constant phase element and R represents resistance. This choice of model allows for a nuanced examination of the conduction behavior. The departure of capacitance from ideal behavior is elucidated through the utilization of a constant phase element (Q), attributed to the coexistence of multiple relaxation processes with comparable periods. The impedance spectroscopy analysis provides valuable insights into the nuanced conduction mechanism within the NFCM nanofiber composites. The observed singular semicircle and the subsequent model fitting contribute to a refined understanding of the electro-active region and the intricate capacitance behavior, furthering the comprehension of the composite material's electrical properties.

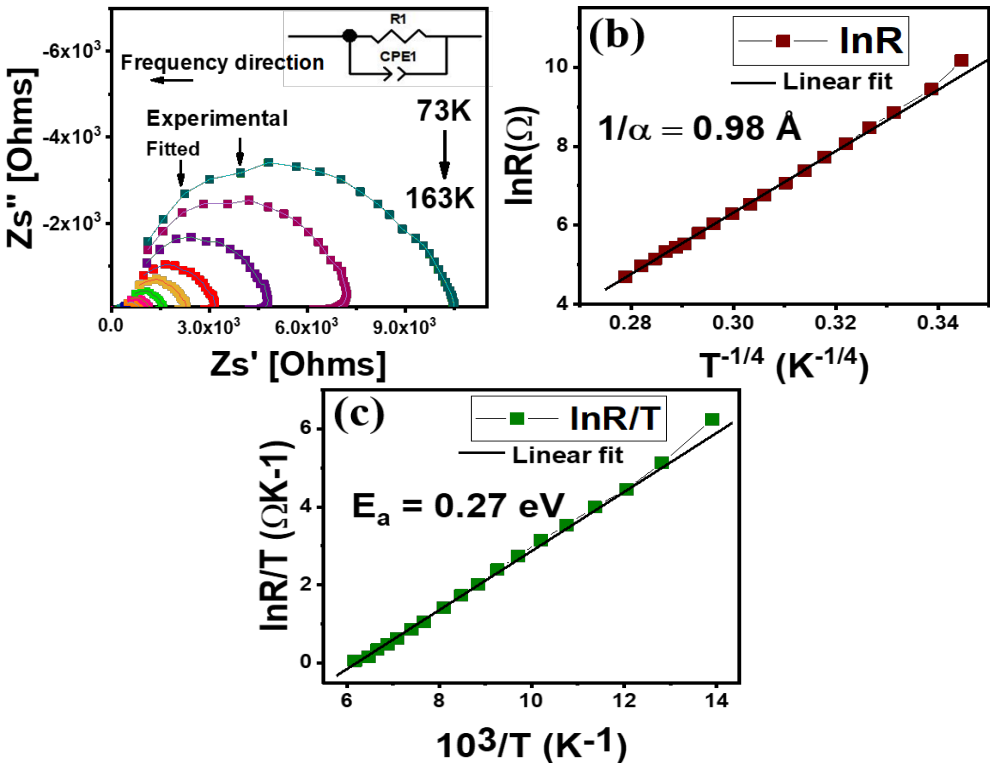

Fig. 4 (a,b,c) depicts the impedance (Z) plane for nanofiber composites of NFCM the manifestation of the MVRH model and the solid lines represent optimal fits to the SPH model.

In the temperature interval spanning 73 K to 163 K, the impedance plot reveals a singular semicircle, indicative of a pronounced relaxation phenomenon within the NFCM composite. Notably, the dominant influence on the conduction mechanism emanates from the NiO/Fe_2O_3 phase. The singular semicircle observed in Fig. 4 (a) implies a predominantly resistive electrical response of the composite within this frequency range, underscoring the prevalence of resistance to

electrical current flow. This behavior may arise from the notable conductivity of the MoS_2 layer or the composite's overall structural arrangement. The semiconducting nature of NiO and Fe_2O_3 components can substantially contribute to the overall resistance, with their concentration and role in the nanofiber composite significantly impacting the observed resistance in the impedance plot. The lower resistance values are attributed to augmented hopping mobility, particularly facilitated by the increased $Fe^{3+} - O - Fe^{2+}$ and $Ni^{2+} - Ni^{3+}$ network [22]. Carbon, particularly in the form of the carbon shell, may bolster the structural integrity of the composite and is likely to exhibit relatively low resistance.

However, its influence on the resistive behavior observed in the impedance plot may be comparatively subdued when contrasted with other semiconducting constituents. The known high electrical conductivity of MoS_2 assumes a pivotal role in contributing to the observed low resistance. MoS_2, serving as a conductive pathway, is anticipated to dominate the electrical response of the composite across the broad frequency range examined [19]. The nuanced interplay of these components underscores the intricate electrical characteristics of the NFCM composite within the specified temperature range.

Table 1. Summary of the fitted factors corresponding to the (R_1Q_1) model for the NFCM nanofiber composite at selected representative temperatures.

T(K)	R_1 (Ω)	Q	n
73	10490	4.29×10^{-10}	0.81
98	4780	1.07×10^{-10}	0.80
113	485	1.01×10^{-10}	0.71
143	170	2.27×10^{-9}	0.66

Based on the equivalent circuit model approach, the resistance R_1 is utilized to illuminate the conduction mechanism. Two distinct models, specifically the MVRH model and the SPH model, were applied across the temperature zone of 73 K to 163 K. The expression for MVRH is as follows:

$$\ln (\rho / \rho_0) = (T_0 / T)^{1/4} \quad (1)$$

Here, ρ_0 represents resistivity, and T_0 is Mott's temperature. The previously mentioned expression for ρ (T) can be represented mathematically as follows:

$$\rho = \rho_0 \exp [2.06(\alpha^3/N(E)\, kT)^{1/4}] \quad (2)$$

$$kT_0 = 18\, \alpha^3/N(E) \quad (3)$$

In this formulation, α is the reciprocal of the localization length, and N(E) signifies the density of states. A physically small confinement length of $1/\alpha$ is achieved when the density of states encompasses the entire value of the e_g electron density. Considering these variables, the equation yields the following result:

$$kT_0 = 171\, \alpha^3 U_m\, \upsilon \quad (4)$$

In this context, υ (lattice volume) is equal to 0.54×10^{-29} m³, and Um (the magnitude of the magnetic potential) is 4 eV, representing their respective values. The expression for SPH is as follows:

$$\ln (\rho / T) = \ln A + W / kT \quad (5)$$

The MVRH model is employed to characterize the hopping of charge carriers in a system where active charge carriers face constraints due to random potential changes [23]. Ideal hopping

arises among sites within a specific energy range. In the temperature zone of 73 K to 163 K, Fig. 4 (a) depicts the plot of resistance (R_1) in contrast to the inverse of temperature, utilizing the MVRH model built on fitted equivalent circuit parameters. The fitting process results in a characteristic temperature T_0 of (7 x 10^6 K) as determined by the variable range model. This information is then used to calculate the localization length ($1/\alpha$), which is found to be 0.98 Å. This distance signifies the nearest-neighbor hopping distance among Fe^{2+} and Fe^{3+} ions at the octahedral site and Ni^{2+} and Ni^{3+} ions. At lower temperatures, where random potential changes are prevalent, active charge carriers are more probable to step with various activation energies, extending farther a distance than their neighboring.

In parallel, the SPH model is used within the temperature range of 73K to 163K, as depicted in Fig. 4 (b). The obtained activation energies (E_a) values of 0.27 eV support the occurrence of Polaronic conduction in this nanofibers composite Fig. 4 (c) [24]. At this temperature, numerous trap centers act as pockets for charge carriers, enhancing the SPH model by facilitating effective connections between Fe^{2+}, Fe^{3+} and Ni^{2+}, Ni^{3+} channels. Analysis based on the fitted data parameters suggests that the MVRH model provides a superior fit compared to the SPH model for the NFCM nanofibers composite. To investigate the temperature-dependent electro-active sites in the composite of NFCM heterostructure nanofibers and appreciate the frequency dependence of M″ and Z″, various electro-active sites were examined. It is important to note that modulus formalism was employed to mitigate electrode polarization effects. In Fig. 5 (a, b), the spectra of Z″ and M″ are depicted, revealing a singular response based on relaxation. Fig. 5 (a) displays a single relaxation peak in the Z″ spectrum within the temperature range of 73 K to 163 K at approximately 10^6 Hz. The relaxation period ($\tau = 1/2\pi f_{max}$) is plotted compared to the temperature, directly proportional to the peak frequency (f_{max}) of Z″. Using the Arrhenius equation, the activation energy of the NFCM heterostructure nanofibers composite is calculated to be 0.24 eV.

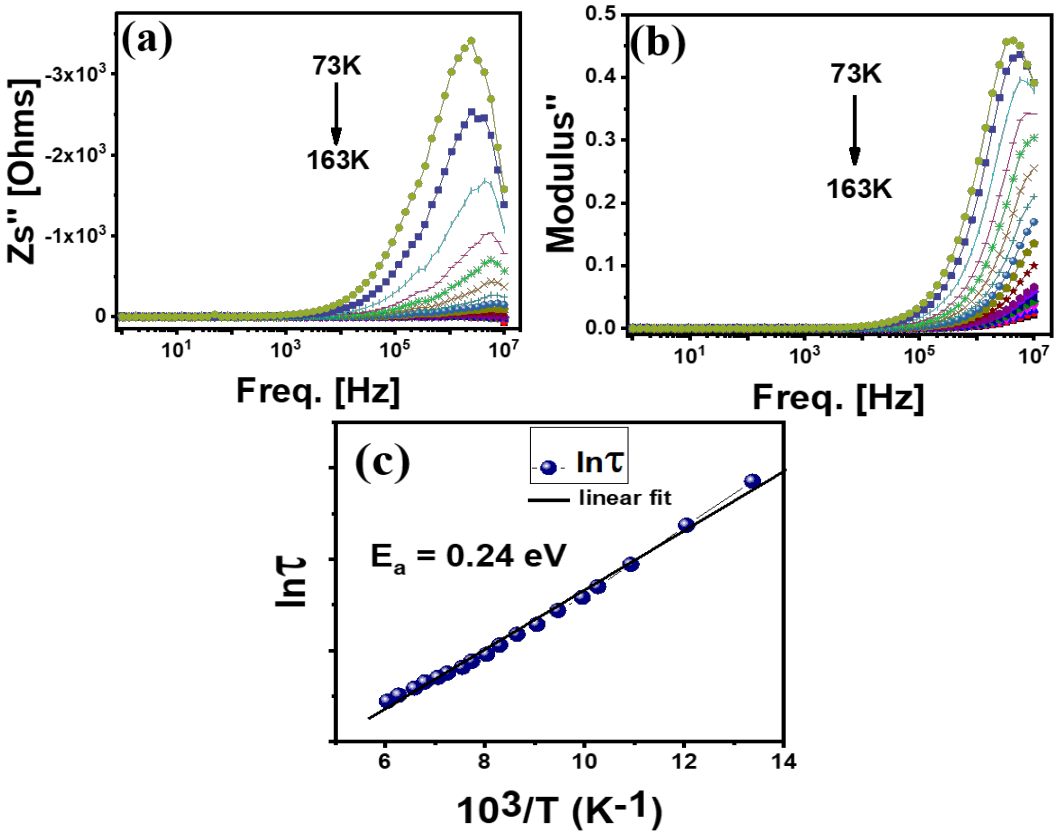

Fig. 5 (a,b,c) shows the frequency-dependent imaginary part of impedance (Z'') and modulus (M''), and the relaxation period is plotted against the inverse of the temperature.

In Fig. 5 (b), a singular relaxation peak is evident in the M″ spectrum within the temperature range of 73 K to 163 K at approximately 10^6 Hz. Notably, the peak frequency shifts from 10^6 Hz to 10^7 Hz as the temperature increases, as depicted in Fig. 5 (a, b). The frequency-dependent electrical spectra of both imaginary part of modulus and impedance offer insights into the relaxation progressions are overseen by the flexibility of short-range or long-range active charge carriers. The noticeable separation in peak frequencies of Z″ and M″ at different temperatures suggests that the flexibility is influenced by the movement of short-range active charge carriers. Conversely, at higher temperatures, the peak frequencies of Z″ and M″ converge, indicating that the mobility of carriers is controlled by the flexibility of long-range charge carriers [26]. Fig. 5(c) presents a logarithmic representation of relaxation time (τ) against the reciprocal of absolute temperature. Following the Arrhenius law, the logarithm of τ demonstrates a linear relationship with T^{-1}, as per the equation $\tau = \tau_0 \exp(-E_a/k\beta T)$, where τ_0, E_a, kβ, and "T" represent the pre-exponential factor, the activation energy of thermally activated processes, Boltzmann constant, and absolute temperature, respectively [27]. The value of peak position, f_{max}, was used to evaluate relaxation time, $\tau (= 1/2\pi f_{max})$, followed by activation energy. As the ambient temperature of the nanofiber composite rises, the relaxation time reduces, as shown in Fig. 5 (c). The linear fit between the data points reveals a reduction in relaxation time as the ambient temperature of the nanofiber composite increases.

The activation energy, calculated from the slope of the linear fit, is established to be 0.24 eV. Fig. 6 (a) illustrates a log-log plot of conductivity versus temperature within the temperature range of 73 K to 163 K. The conductivity plot unveils a frequency-independent conductivity region at lower frequencies, transitioning into frequency-dependent conductivity at higher frequencies. Notably, as the temperature increases, the frequency at DC conductivity transforms into AC conductivity and shifts towards higher frequencies. This shift signifies the hopping of active charge carriers in the NFCM heterostructure nanofibers composite. The observed increasing trends in conductivity with frequency for all temperatures indicate that the presence of hopping channels is essential for hopping conduction. The higher frequency stimulates the opening of these channels, facilitating the hopping of electrons and holes between the $Fe^{3+} \rightarrow Fe^{2+}$ and $Ni^{2+} \rightarrow Ni^{3+}$ ions, respectively [28]. When conductivity is frequency-dependent, the behavior can be elucidated by the equation: $(\omega) = \sigma_0 + A\omega^s$, where angular frequency (2πf) is denoted by "ω," AC conductivity is represented by "σ(ω)," DC conductivity is represented by "σ_0," the pre-exponential factor is represented by "A," and the slope is represented by "s" [29]. With increasing temperature, the pre-exponential factor (A), determining the strength of polarizability, rises, leading to a rise in polarizability and dielectric properties. The electrical conductivity of NFCM nanofibers material is measured as 2.1×10^{-4} S/cm. This conductivity may result from doping effects, electron density shifts, and matrix expansion induced by the effective integration of NiO and Fe_2O_3 nanofibers into the MoS_2 matrix.

In Fig. 6 (b), a conductivity plot is presented at a frequency of 10^7 Hz across various temperatures. Utilizing the Arrhenius model, the activation energy is computed, yielding a value of 0.2 eV. This determination aligns with the activation energies derived from impedance, relaxation constants, and the SPH model. At lower temperatures, the majority of carriers, lacking the energy required to fulfill the potential, are situated in the charged space zone. The discernibly distinct activation energies for conduction and relaxation processes are associated with the integration of hopping energy, disorder, and polaron into the conduction mechanism.

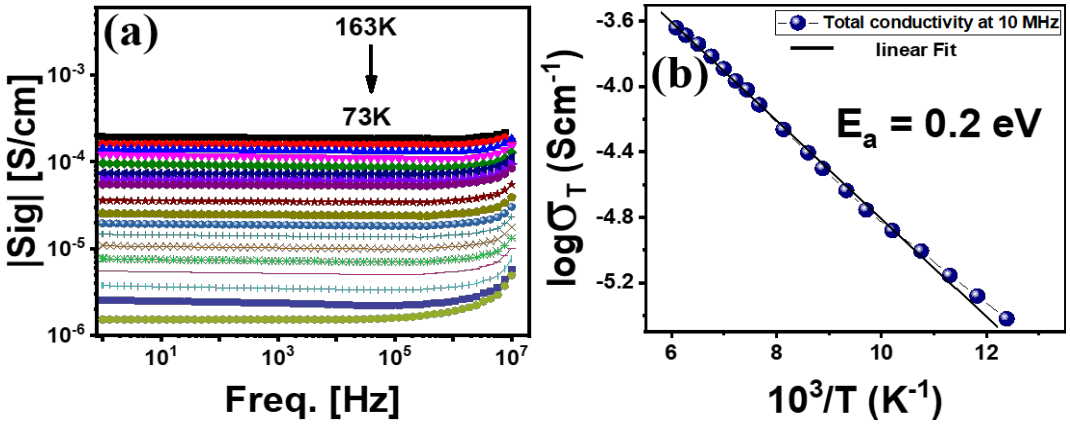

Fig. 6. (a,b) Variation of the AC conductivity (σ) as a function of frequency and total conductivity for NFCM nanofibers composite at 10 MHz at all temperatures.

Fig. 7 (a) illustrates the temperature-dependent real component of the dielectric constant spanning the temperature range of 73K to 163K. These plots reveal the existence of diverse polarizations within the NFCM nanofibers material, encompassing interfacial, atomic, electronic, and dipolar polarization In conducting composites, polaron and bipolaron represent the two primary charge carrier types. A heightened dielectric to localized or immobilized dipoles that can traverse extensive distances, predominantly observable at low frequencies [30]. As depicted in Fig. 7 (a), the dielectric constant experiences an increase at lower temperatures, indicating the polarization of dipoles at these frequencies over sufficient time. In the high-frequency domain, the dielectric constant diminishes with temperature. This reduction with rising frequency is attributed to the dipoles lagging behind the applied AC field based on their mobility. The rotational displacement of these dipoles prevents them from adequately tracking the AC field around the relaxation frequency, resulting in a significant reduction in the dielectric constant of around 10^5 Hz [31]. The presence of highly conductive materials such as MoS_2 and carbon can influence the dielectric constant. Materials with elevated electrical conductivity can efficiently dissipate electric fields, potentially leading to a lower dielectric constant. In this scenario, MoS_2 and carbon may exert dominance over the electrical response, contributing to the observed decrease in the dielectric constant.

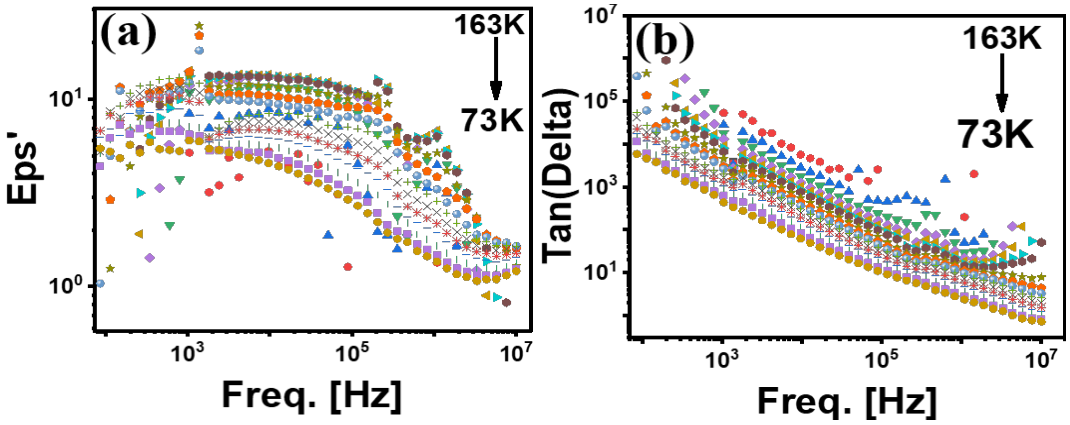

Fig. 7. (a,b) the dielectric constant (ε) and dielectric loss (tanδ) for NFCM nanofibers composites.

Elevated values of tangent loss are notably observed at lower frequencies during the polarization process, stemming from the alignment shift of these dipoles (short-range migration), as depicted in Fig. 7 (b). The interfaces within the nanofiber composite can induce losses due to interfacial polarization, contributing to a pronounced tangent loss at low frequencies. Defects within the composite may introduce additional loss mechanisms, resulting in heightened tangent loss and potential disruption of the composite's regular electrical behavior. The relaxation process induces a decline in the dielectric constant at higher frequencies due to the clustering of NiO nanofibers into the MoS_2 conducting matrix. Within this frequency range, the electric field undergoes directional changes before the dipoles line up themselves with the field, achieving frequency independence and consequently yielding a reduced dielectric loss [32].

The interaction between the electronic structures of Ni^{2+} and Fe^{3+} ions in the matrix can have a considerable impact on the electrical characteristics of a composite when NiO (nickel oxide) and Fe_2O_3 (iron oxide) are integrated as nanofibers. Ni^{2+} (Nickel Ion) has the electrical configuration [Ar] $3d^4$. This indicates that the partially filled d-orbitals of nickel ions in the NiO structure permit some electrical conductivity because electrons can flow between these orbitals. Iron ion Fe^{3+} has the electrical configuration [Ar] $3d^5$. Half-filled d-orbitals, as opposed to partially or fully filled ones, are less conductive and more stable in this arrangement. Nickel oxide (NiO) is a p-type semiconductor. The conductivity in NiO is mainly caused by holes, or positive charge carriers, which are produced in the valence band by partial filling of the 3d orbital of NiO [33] .These holes allow electrons to jump between Ni^{3+} sites, which increases electrical conductivity. However, because of the stable, half-filled 3d orbitals of Fe^{3+}, Fe_2O_3 (hematite) is a poor conductor. Compared to Ni^{2+} ions, Fe^{3+} ions are less likely to take part in conduction activities because of their more stable electronic structure. The electrical characteristics of the composite are mostly determined by the interaction between the Ni^{2+} and Fe^{3+} ions when NiO is introduced into Fe_2O_3 nanofibers. Ni^{2+} ions are accountable for electrical conductivity because they permit electron hopping between partially filled 3d orbitals, however, when Fe^{3+} ions are present, the electron hopping mechanism is impeded. Fe^{3+} ions, with their half-filled 3d orbitals, tend to trap or lock electrons, making them less mobile. This decrease in overall charge mobility in the material results in an increase in the resistivity of the composite. Fe^{3+} ions with a half-filled d^5 configuration create a more localized electron environment [34]. The electrons in Fe^{3+} ions are more stable and less likely to engage in electron hopping, particularly when interacting with Ni^{2+} ions. Because the Fe^{3+} ions efficiently trap electrons, the introduction of NiO into Fe_2O_3 nanofibers results in decreased electron mobility and increased resistivity or more insulating behavior in the composite. Semiconducting and insulating properties will probably coexist in the composite of NiO/Fe_2O_3 nanofibers. The Fe_2O_3 phase will counterbalance this by trapping electrons and lowering total charge carrier mobility, but the NiO phase will contribute to some degree of conductivity. The electrical characteristics of the composite are largely determined by this interaction between the d-orbitals of Ni $^{3+}$ and Fe^{2+}. The electron locking action of Fe^{3+} ions results in a decrease in electrical conductivity. Because the Fe^{2+} and Fe^{3+} states, which predominate in the Fe_2O_3 structure, impede the flow of charge carriers (electrons), the overall resistivity increases [35].

Within the X-band frequency range, the total shielding efficiency was quantified using a vector network analyzer, employing scattering parameters. Taking into consideration the SE_R, SE_A, and SE_T may be explained as follows by using equations 13, 14 and 15 [36].

$$SE_T \ (dB) = SE_A + SE_R + SE_{MR} \tag{6}$$

$$SE_T \ (dB) = SE_A + SE_R \tag{7}$$

$$R = |S_{11}^2| + |S_{22}^2| \tag{8}$$

$$T = |S_{12}^2| + |S_{21}^2| \tag{9}$$

$$T + R + A = 1 \tag{10}$$

$$A = 1 - R - T \tag{11}$$

$$A_{eff} = \frac{1-T-R}{1-R} \quad (12)$$

In order to account for the effective power of the incoming electromagnetic wave inside the shield material, the SE_R, SE_A, and SE_T can be expressed as follows [37].

$$SE_A = -10\ \mathrm{Log}(1 - A_{eff}) \quad (13)$$

$$SE_R = -10\ \mathrm{Log}(1 - R) \quad (14)$$

$$SE_T = -10\ \mathrm{Log}\ T \quad (15)$$

These phenomena can be elucidated by the intricate microstructure of the material, encompassing conductive properties (C), magnetic constituents (Fe, Co), and dielectric loss mechanisms affecting electromagnetic waves [38]. Furthermore, the distinctive attributes of cobalt ferrite nanofibers, such as their elevated surface area-to-volume ratio, enhanced permeability and conductivity, structural integrity, and adjustability, collectively contribute significantly to augmenting their effectiveness of EMI shielding. Among all the scrutinized samples, S_1 exhibited the most superior shielding characteristics, as indicated by the conducted analysis. The results suggest that low-temperature sintering yields additional advantages in terms of effective EMI shielding.

Using Equations (13), (14), and (15) enables the determination of SE_R, SE_A, and SE_T values across the energy spectrum. A material exhibiting a substantial reflection coefficient (R) may both reflect and scatter incoming waves, while a material with a significant absorption coefficient (A) may dissipate electromagnetic energy due to resistive losses [39]. Fig. 8 (a) illustrates the shielding efficacy of three distinct samples NFCM nanofiber composites as a function of frequency, with a specific focus on their absorption properties within the X-band range. The shielding effectiveness (SE_A) for all three nanofiber samples exhibits an ascending trend with increasing frequency, indicating a notable enhancement in the Specific Energy Absorption (SE_A) of the nanofiber samples attributed to heightened absorption losses [40].

Simplified, at elevated frequencies, the nanofibers exhibit an increased capability to absorb electromagnetic radiation, resulting in heightened shielding effectiveness. Fig. 8 (b) portrays the shielding efficiency arising from the X-band reflection of electromagnetic waves, illustrating its frequency dependence for different samples of NFCM nanofibers. Notably, the 3 mm thick nanofiber composite displays the most significant SE_R values, indicating that electromagnetic wave absorption constitutes the primary shielding mechanism for NFCM nanofibers [41]. Upon comprehensive analysis of each sample, the absorption-induced shielding effectiveness (SE_A) surpasses the reflection-induced shielding effectiveness (SE_R). The aggregate assessment across all samples reveals that the shielding achieved through absorption (SE_A) prevails over that achieved through reflection (SE_R). The intricate microstructure of the system, encompassing dielectric characteristics (NiO), conductive materials (MoS_2, C), and magnetic components (Ni, Fe), sheds light on these mechanisms, contributing to various electromagnetic wave loss mechanisms. In Fig.(c) the histogram for SE_A, SE_R and SE_T is displayed by varying thickness from 1 to 3 mm

The elevated shielding results are likely attributed to the outermost MoS_2 layer, renowned for its exceptional electrical conductivity and EMI shielding properties [20]. Functioning as a conducting coating, MoS_2 is pivotal in effectively attenuating EMI by redirecting and dissipating electromagnetic waves. While the core $(NiO)_{(0.5)}/(Fe_2O_3)_{(0.5)}$ contributes magnetic properties, and the carbon (C) shell enhances nanofiber structural integrity, it is the conducting MoS_2 coating that plays a crucial role in EMI shielding interference. MoS_2's high conductivity enables efficient absorption and redirection of electromagnetic radiation, serving as a key factor in the observed high shielding results in this nanofiber material [42].

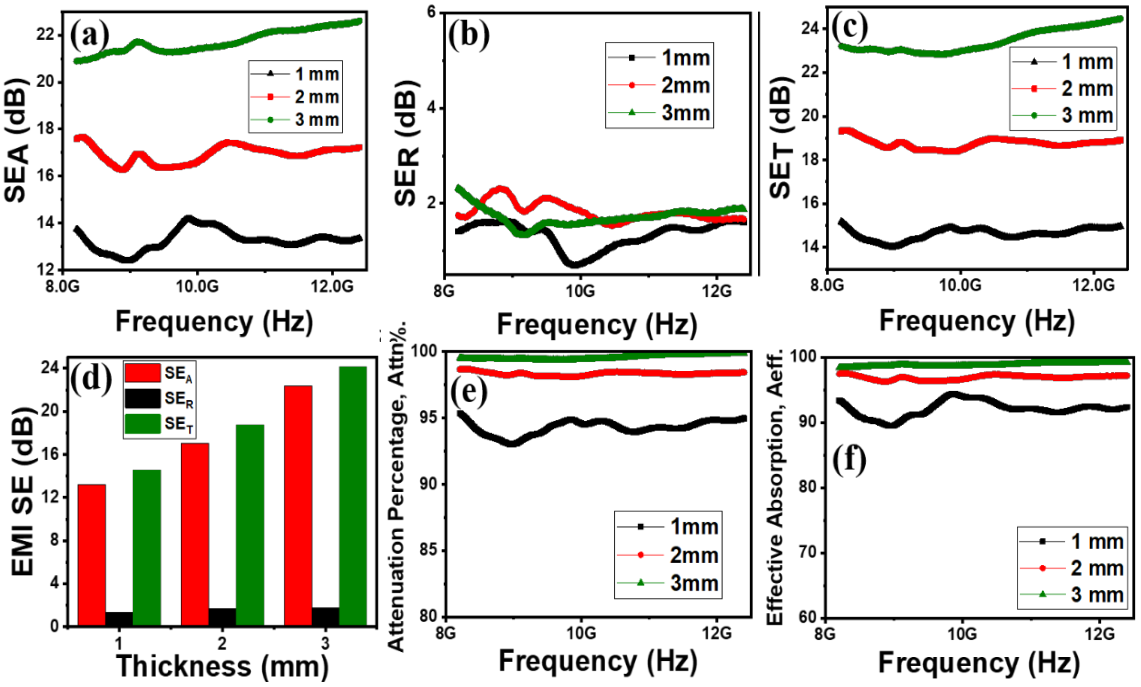

Fig. 8 (a,b,c) displays the shielding efficiency (SE) due to absorption (SE_A), reflection (SE_R), and total EMI shielding effectiveness (SE_T). (d,e,f) display histogram for SE_A SE_R SE_T, the percentage attenuation and percentage of effective absorption.

EMI shielding mechanism. In the X-band frequency spectrum, a peak SE_T value of 24.25 dB is achieved, corresponding to a thickness of 3 mm. The material NFCM nanofibers are suggested as a viable option for EMI shielding in light of the results mentioned above, which could lead to new opportunities for basic research and applications. The total shielding effectiveness (SE_T) registers at approximately 14.8 dB (95% attenuation) for a 1 mm thick sample, demonstrating an escalating trend with increasing thickness, as depicted in Fig. 8(c). The thickness-dependent trends in SE_A, SE_R, and SE_T are visually represented using a histogram, illustrating data acquired at a frequency of 10.1 GHz (Fig. 8 (d)).

Table 2. Compares the overall shielding efficacy and the percentage of attenuation for various thicknesses of the NFCM nanofiber material.

Thickness of sample (mm)	SE_T (dB)	Attenuation percentage
1	14.89	95.18
2	18.87	98.30
3	24.25	99.33

The absorption quantifies the reduction in the strength or intensity of the incident electromagnetic wave upon traversing the shielding material. The active absorption percentage, denoting the portion of input electromagnetic energy absorbed and scattered by the shielding material, is a key metric. Variations in attenuation % and effective absorption percentage across different samples concerning frequency within the X-band are presented in Fig. 8 (e) and 5.8 (f). Fig. 8 (e) illustrates the total power absorbed by the EMI shielding material, referred to as effective absorption, achieving an impressive attenuation percentage of 99.3%. These outcomes underscore exceptional shielding characteristics, emphasizing the dominance of an absorption-driven shielding mechanism.

4. Conclusions

In this work, two processes that combines electrospinning and simple hydrothermal techniques is used for the synthesis of NFCM nanofibers composite. The resulting composites exhibit facile synthesis, ensuring high-quality outcomes and stability. Structural and morphological attributes are scrutinized using XRD and FE-SEM techniques. A thorough investigation of the electro-active regions within the NFCM nanofibers composite is conducted, unveiling insights into its temperature-dependent conduction mechanisms using impedance spectroscopy. The material's impedance and relaxation characteristics find optimal explication through the MVRH model, predicated on equivalent circuit model attributes. The anticipated activation energy, derived from the electro-active region, stands at 0.24 eV. The as-synthesized NFCM nanofibers composite, holding promise for critical applications, showcases good EMI shielding performance, predominantly driven by an absorption-centric in the x-band frequency range.

Funding

Researchers supporting project number (RSPD2025R741), King Saud University.

Acknowledgement

The authors would like to thank the Researchers Supporting Project number (RSPD2025R741), King Saud University, Riyadh, Saudi Arabia.

References

[1] U. Anwar et al., Mater. Today Commun., vol. 39, no. April, p. 109023, 2024; https://doi.org/10.1016/j.mtcomm.2024.109023

[2] O. Farooq, M. Anis-ur-Rehman, A. ul Haq, J. Alloys Compd., vol. 786, pp. 314-320, 2019; https://doi.org/10.1016/j.jallcom.2019.01.347

[3] G. Korotcenkov, Nanomaterials, vol. 11, no. 6, pp. 21-24, 2021; https://doi.org/10.3390/nano11061544

[4] C. Han, M. Zhang, W. Q. Cao, M. S. Cao, Carbon N. Y., vol. 171, pp. 953-962, 2021; https://doi.org/10.1016/j.carbon.2020.09.067

[5] N. Angel, L. Guo, F. Yan, H. Wang, L. Kong, J. Agric. Food Res., vol. 2, p. 100015, 2020; https://doi.org/10.1016/j.jafr.2019.100015

[6] O. Farooq, M. Anis-Ur-Rehman, A. Ul Haq, Mater. Res. Express, vol. 7, no. 1, pp. 0-9, 2020; https://doi.org/10.1088/2053-1591/ab5536

[7] M. Rafi, U. Anwar, M. H. Alnasir, A. Ramzan, A. Noor, S. Mumtaz, Ceram. Int., no. April, 2024; https://doi.org/10.1016/j.ceramint.2024.07.229

[8] N. Sheoran, V. Kumar, A. Kumar, Structural, Magnetic, Dielectric and Energy Storage Analysis of CoFe2O4@BaTiO3 and BaTiO3@CoFe2O4 Core-Shell Nano- Composites, pp. 1-23, 2020; https://doi.org/10.21203/rs.3.rs-33291/v1

[9] D. Yin, J. Liu, X. Bo, L. Guo, Cobalt-iron selenides embedded in porous carbon nanofibers for simultaneous electrochemical detection of trace of hydroquinone, catechol and resorcinol, Anal. Chim. Acta, vol. 1093, no. xxxx, pp. 35-42, 2020; https://doi.org/10.1016/j.aca.2019.09.057

[10] Z. Wang, J. Hai, T. Li, E. Ding, J. He, B. Wang, ACS Sustain. Chem. Eng., vol. 6, no. 8, pp. 9921-9929, 2018; https://doi.org/10.1021/acssuschemeng.8b01166

[11] J. Wang et al., Carbon N. Y., vol. 165, pp. 275-285, 2020; https://doi.org/10.1016/j.carbon.2020.04.090

[12] J. Xu, L. Li, F. He, R. Lv, P. Yang, Electrochim. Acta, vol. 148, pp. 211-219, 2014; https://doi.org/10.1016/j.electacta.2014.10.061

[13] N. A. Noor, U. Anwar, A. Mahmood, Chem. Phys. Lett., vol. 739, no. December 2019, p. 137031, 2020; https://doi.org/10.1016/j.cplett.2019.137031

[14] J. Prasad et al., ACS Appl. Mater. Interfaces, vol. 12, no. 36, pp. 40828-40837, 2020; https://doi.org/10.1021/acsami.0c06219

[15] B. Wang, G. Wang, X. Cheng, H. Wang, Chem. Eng. J., vol. 306, pp. 1193-1202, 2016; https://doi.org/10.1016/j.cej.2016.08.057

[16] F. Niu et al., Chem. Eng. J., vol. 453, no. P2, p. 139933, 2023; https://doi.org/10.1016/j.cej.2022.139933

[17] Z. Masoumi et al., ACS Appl. Mater. Interfaces, vol. 13, no. 33, pp. 39215-39229, 2021; https://doi.org/10.1021/acsami.1c08139

[18] Z. Tong et al., Carbon N. Y., vol. 179, pp. 646-654, 2021; https://doi.org/10.1016/j.carbon.2021.04.051

[19] A. P. Guo, X. J. Zhang, S. W. Wang, J. Q. Zhu, L. Yang, G. S. Wang, Chempluschem, vol. 81, no. 12, pp. 1305-1311, 2016; https://doi.org/10.1002/cplu.201600370

[20] J. Prasad, A. K. Singh, K. K. Haldar, V. Gupta, K. Singh, J. Alloys Compd., vol. 788, pp. 861-872, 2019; https://doi.org/10.1016/j.jallcom.2019.02.246

[21] C. Yazirin, P. Puspitasari, M. I. N. Sasongko, D. I. Tsamroh, P. Risdanareni, AIP Conf. Proc., vol. 1887, no. September, 2017; https://doi.org/10.1063/1.5003521

[22] S. Jana, A. Mondal, A. Ghosh, Appl. Catal. B Environ., vol. 232, pp. 26-36, 2018; https://doi.org/10.1016/j.apcatb.2018.03.038

[23] M. V. S. Kumar, G. J. S. E. Melagiriyappa, K. K. N. H. S. Jayanna, J. Mater. Sci. Mater. Electron., vol. 29, no. 15, pp. 12795-12803, 2018; https://doi.org/10.1007/s10854-018-9398-0

[24] S. Ahmed et al., J. Alloys Compd., vol. 883, p. 160875, 2021; https://doi.org/10.1016/j.jallcom.2021.160875

[25] S. Javaria et al., J. Magn. Magn. Mater., vol. 563, no. September, p. 170037, 2022; https://doi.org/10.1016/j.jmmm.2022.170037

[26] D. C. Sinclair, A. R. West, J. Appl. Phys., vol. 66, no. 8, pp. 3850-3856, 1989; https://doi.org/10.1063/1.344049

[27] L. Liu et al., Appl. Phys. A Mater. Sci. Process., vol. 104, no. 4, pp. 1047-1051, 2011; https://doi.org/10.1007/s00339-011-6358-4

[28] A. B. Abou Hammad, A. G. Darwish, A. M. El Nahrawy, Appl. Phys. A Mater. Sci. Process., vol. 126, no. 7, pp. 1-12, 2020; https://doi.org/10.1007/s00339-020-03679-z

[29] M. Younas et al., Phys. Chem. Chem. Phys., vol. 16, no. 30, pp. 16030-16038, 2014; https://doi.org/10.1039/C4CP00951G

[30] J. Bisquert, G. Garcia-Belmonte, Russ. J. Electrochem., vol. 40, no. 3, pp. 352-358, 2004; https://doi.org/10.1023/B:RUEL.0000019676.99599.bc

[31] R. A. Sutar, L. Kumari, M. V. Murugendrappa, Phys. B Condens. Matter, vol. 573, no. July, pp. 36-44, 2019; https://doi.org/10.1016/j.physb.2019.07.011

[32] J. Cheng et al., J. Mater., vol. 7, no. 6, pp. 1233-1263, 2021; https://doi.org/10.1016/j.jmat.2021.02.017

[33] S. Zhang et al., Beilstein J. Nanotechnol., vol. 10, pp. 1923-1932, 2019; https://doi.org/10.3762/bjnano.10.188

[34] B. Quan et al., Adv. Funct. Mater., vol. 29, no. 28, pp. 1-10, 2019; https://doi.org/10.1002/adfm.201901236

[35] Y. Shen et al., Ceram. Int., vol. 46, no. 9, pp. 13397-13406, 2020; https://doi.org/10.1016/j.ceramint.2020.02.121

[36] H. R. Kim, B. S. Kim, I. S. Kim, Mater. Chem. Phys., vol. 135, no. 2-3, pp. 1024-1029, 2012; https://doi.org/10.1016/j.matchemphys.2012.06.008

[37] M. M. Ismail, S. N. Rafeeq, J. M. A. Sulaiman, A. Mandal, Appl. Phys. A Mater. Sci. Process., vol. 124, no. 5, p. 0, 2018; https://doi.org/10.1007/s00339-018-1808-x

[38] M. F. Shakir et al., SN Appl. Sci., 2020; https://doi.org/10.1007/s42452-020-2535-4

[39] Y. Cheng, W. Zhu, X. Lu, C. Wang, Compos. Commun., vol. 27, no. April, p. 100823, 2021; https://doi.org/10.1016/j.coco.2021.100823

[40] C. Wan, J. Li, Carbohydr. Polym., vol. 161, pp. 158-165, 2017; https://doi.org/10.1016/j.carbpol.2017.01.003

[41] F. Mederos-Henry et al., Nanomaterials, vol. 9, no. 9, 2019; https://doi.org/10.3390/nano9091196

[42] S. V. Dravid, S. D. Bhosale, S. Datar, R. K. Goyal, Nickel Nanoparticle-Filled High-Performance Polymeric Nanocomposites for EMI Shielding Applications, 2019; https://doi.org/10.1007/s11664-019-07535-6